



Defect-band bridge photothermally activates Type III heterojunction for CO₂ reduction and typical VOCs oxidation

Jingwei Li^a, Jianrui Feng^b, Xiaomin Guo^a, Hongli Fang^a, Jiayi Chen^a, Churong Ma^c,
Ruchun Li^{d,e}, Yuya Wang^a, Zebao Rui^{a,*}

^a School of Chemical Engineering and Technology, The Key Laboratory of Low-carbon Chemistry & Energy Conservation of Guangdong Province, Guangdong Engineering Technology Research Center for Platform Chemicals from Marine Biomass and Their Functionalization, Sun Yat-sen University, Zhuhai 519082, China

^b Department of Chemistry, Zhejiang University, Hangzhou 310058, China

^c Guangdong Provincial Key Laboratory of Optical Fiber Sensing and Communications, Institute of Photonics Technology, Jinan University, Guangzhou 511443, China

^d State Key Laboratory of Advanced Technology for Materials Synthesis and Processing, Wuhan University of Technology, Wuhan 430070, China

^e Foshan Xianhu Laboratory of the Advanced Energy Science and Technology Guangdong Laboratory, Xianhu hydrogen Valley, Foshan 528200, China

ARTICLE INFO

Keywords:

Type III heterojunction
WO_{3-x}/GdCrO₃
Defect-band state
CO₂ reduction
VOCs degradation

ABSTRACT

This work reports a novel strategy to activate type III heterojunction through introducing defect sites at the interfaces and making use of the defect band as the bridge for storage, secondary excitation, and interband transfer of the photothermal induced charges for constructing two-component Type B heterojunction photothermocatalyst. Type III heterojunction WO_{3-x}/GdCrO₃ is activated by defect-band state W^{5+/4+} at WO_{3-x} interface under photothermal conditions, achieving efficient charge separation, high redox potential, and full visible light absorption. The as-bridged (or Type B) heterojunction WO_{3-x}-R/GdCrO₃ as non-noble metal catalyst demonstrates excellent photothermocatalytic performance in toluene degradation with a reaction rate five times higher than that of WO_{3-x}/GdCrO₃ with less interfacial defect sites as well as in CO₂ reduction with high CO and CH₄ yielding rates of 49.6 μmol g⁻¹ h⁻¹ and 18.5 μmol g⁻¹ h⁻¹ in gas-solid reaction system without sacrifice agent, evidently better than those reported in the literature.

1. Introduction

Photocatalytic or photothermocatalytic performance of the catalysts for energy and environmental applications, such as the reduction or reuse of green gas CO₂ and degradation of harmful volatile organic compounds (VOCs), are positively correlated with their light response range, carriers separation efficiency, and redox potentials [1,2]. The heterojunction photocatalysts or photothermocatalysts composed by the semiconductor composites have been extensively studied due to their great potential for obtaining these properties and fully making use of the sunlight [3], especially those with overlapped heterointerfaces and suitable band positions among the composites, such as Type II, Z-scheme, and S-scheme heterojunctions [3–7]. However, a trade-off among light response range, redox potentials, and requirement of bandgaps overlap restricts the performance improvement of these mainstream photocatalytic, photothermocatalytic or photoelectrochemical heterojunction catalysts [3–8].

By comparing, Type III heterojunctions, without the requirement for

bandgaps overlap, can be constructed by a large class of semiconductors, including those with strong redox ability and wide light response range characters. For example, Type III heterojunction Ag₃PO₄/GdCrO₃ was recently activated by introducing plasmonic Ag nanoparticles (NP) as the bridge for photoinduced charges transfer to construct Type B heterojunction Ag₃PO₄/Ag/GdCrO₃ and achieved satisfied photothermocatalytic performance for VOCs degradation and CO₂ reduction, which represented the first activation and photocatalytic application of Type III heterojunction [8]. However, the application potential of Type III heterojunctions in the field of photocatalysis and photothermocatalysis is still challenge due mainly to the suppressed interband charges transfer and separation. For example, the Type III heterojunction WO₃/GdCrO₃ reported in our recent work showed poor photoinduced charges transfer and separation between components and a low photothermocatalytic CO₂ reduction rate with low CO and CH₄ yielding rates of 1.3 μmol g⁻¹ h⁻¹ and 1.8 μmol g⁻¹ h⁻¹ under visible light irradiation and 363 K [9]. In spite of the encouraged performance of the plasmonic Ag NP bridged Type III (or Type B) heterojunction

* Corresponding author.

E-mail address: ruizebao@mail.sysu.edu.cn (Z. Rui).

<https://doi.org/10.1016/j.apcatb.2022.121248>

Received 2 December 2021; Received in revised form 14 February 2022; Accepted 21 February 2022

Available online 25 February 2022

0926-3373/© 2022 Elsevier B.V. All rights reserved.

photothermocatalysts [8,9], the additional noble metal Ag consumption, high thermal energy input requirement (e.g., not less than 363 K for $\text{Ag}_3\text{PO}_4/\text{Ag}/\text{GdCrO}_3$ and $\text{WO}_3/\text{Ag}/\text{GdCrO}_3$) for stimulating the transfer of the charges, and the careful design requirement of the two interfaces (semiconductor-NP-semiconductor) restricts their catalytic application.

Defect-rich semiconductors, e.g., WO_{3-x} , MoO_{3-x} , and Cu_{2-x}Te , with rich excessive electrons on its defect sites exhibited localized surface plasmon resonance (LSPR) effect like plasmonic metal (e.g., Ag, Au, Cu) through the excitation of excessive electrons [10–15]. LSPR effect of the defect-rich semiconductors could extend their light response to near infrared range with enhanced light conversion efficiency and increase the charges separation efficiency [16–21]. For instance, the ultrathin $\text{W}_{18}\text{O}_{49}$ (WO_{3-x}) nanowires reported by Ye's group showed strong LSPR-induced visible-near-infrared light absorption and well photocatalytic CO_2 reduction performance [21]. The LSPR characteristics of defect-rich semiconductors imply a possibility to directly activate Type III heterojunctions through careful design of the defects without the additional requirement of plasmonic metals for photocatalytic or photothermocatalytic applications.

This work reports, for the first time, a facile strategy to activate the Type III heterojunction for constructing a robust Type B heterojunction photothermocatalyst through introducing defect sites at the interfaces and making use of the defect band as the bridge for storage, secondary excitation, and interband transfer of the photothermal induced charges. Bandgap broken Type III heterojunction $\text{WO}_{3-x}/\text{GdCrO}_3$ with high redox potentials, narrow bandgaps, and tunable interfacial defects is chosen as an example of proof [8,19,22]. After introducing rich interfacial $\text{W}^{5/4+}$ defect sites for constructing $\text{WO}_{3-x}\text{-R}/\text{GdCrO}_3$, the LSPR of the captured photogenerated electrons at the $\text{W}^{5/4+}$ defect-band under photothermal conditions can induce the hot electrons transit from Fermi level hybrid orbit $5d_{t_z}/O\ 2p_y + 2p_z$ to a higher energy level to capture the photogenerated holes at the valance band of GdCrO_3 , achieving efficient carriers separation and full light response at no cost of the high photoredox potentials. The as-developed defect band bridged (or Type B) heterojunction $\text{WO}_{3-x}\text{-R}/\text{GdCrO}_3$ exhibits excellent photothermocatalytic performance in both CO_2 reduction and VOCs degradation with remarkably higher reaction rate than the mainstream photocatalysts. This work will bring a new research and development interest in designing next generation heterojunction catalysts for future environmental and energy catalysis.

2. Experimental section

2.1. Material synthesis

The GdCrO_3 was firstly prepared with a solid-state synthesis method. Typically, 10 mmol of $\text{Gd}(\text{NO}_3)_3 \cdot 6\text{H}_2\text{O}$ (Macklin, AR), 10 mmol of $\text{Cr}(\text{NO}_3)_3 \cdot 9\text{H}_2\text{O}$ (Aladdin, AR), and 120 mmol of CON_2H_4 (Aladdin, AR) were ground uniformly and then calcined at 850°C for 3 h in air to obtain the GdCrO_3 powder. 0.78 mmol of GdCrO_3 was uniformly dispersed in 30 mL of 0.029 mol L^{-1} WCl_6 (Sian Biochemical Technology Co., LTD, AR) absolute ethanol solution under strong stirring. The mixture solution was then transferred into a Teflon-lined stainless-steel autoclave with a volume of 100 mL and heated at 200°C for 24 h. The as-obtained powders were collected, washed with ethanol, and dried overnight at $\sim 100^\circ\text{C}$ to obtain the defect sites enriched $\text{WO}_{3-x}/\text{GdCrO}_3$ (or $\text{WO}_{3-x}\text{-R}/\text{GdCrO}_3$). The obtained $\text{WO}_{3-x}\text{-R}/\text{GdCrO}_3$ was then treated by 30 wt% H_2O_2 solution for 30 min to obtain the $\text{WO}_{3-x}/\text{GdCrO}_3$ with less defect sites. The defect sites enriched WO_{3-x} (or $\text{WO}_{3-x}\text{-R}$) was prepared with the same process of $\text{WO}_{3-x}\text{-R}/\text{GdCrO}_3$ without the addition of GdCrO_3 . The WO_{3-x} was prepared by treating the $\text{WO}_{3-x}\text{-R}$ with 30 wt% H_2O_2 solution for 30 min. All the samples were dried at $\sim 100^\circ\text{C}$ overnight before tests and characterizations.

2.2. Characterizations

The morphology of the catalysts was checked by emission scanning electron microscopy (SEM, Quanta 400 F) and transmission electron microscopy (TEM, F30 model FEI Tecnai G2 F30). The crystal structure of the samples was analyzed by D8 ADVANCE Powder diffractometer for obtaining X-ray diffraction (XRD) patterns and Laser Micro-Raman Spectrometer (Renishaw inVia). The electronic structures and optical properties were tested by ultraviolet-visible (UV-vis) diffuse reflectance spectrophotometer (DRS, UV-3600), X-ray photoelectron spectroscopy (XPS) spectroscopy (ESCALAB 250, Thermo-VG Scientific) equipped with a monochromatic $\text{Al K}\alpha$ X-ray source with a photon energy of 1486.6 eV under a vacuum degree of $\sim 2 \times 10^{-9}$ Pa, and electron spin resonance (ESR) spectrometer (Bruker model A300). The binding energies were corrected by adjusting the main C 1s peak of the carbon surface deposit to a position of 284.8 eV. The photothermal synergistic properties were analyzed based on the related characterizations from the infrared imaging device (testo 869), the electrochemical setup (CHI660E) coupled with a Xe lamp, the femtosecond-nanosecond transient absorption (TA) spectrometer (Helios Fire), and the finite-difference-time-domain (FDTD) simulations (Lumerical Solutions Inc. Software). Mott-Schottky (MS) measurements were tested on the electrochemical workstation (CHI660E). The Ag/AgCl electrode and 1.0 mol L^{-1} of Na_2SO_4 (pH = 7.0) were used as the reference electrodes and electrolyte, respectively.

2.3. Catalytic performance evaluations

Photothermocatalytic VOCs oxidation was tested in a stainless-steel batch reactor coupled with a thermode and light source ($\lambda = 420\text{--}780\text{ nm}$, 400 mW cm^{-2}), as illustrated in Fig. S1 (Supporting information). The real temperature of the photocatalyst during the reaction was measured by setting a thermoelement directly on the light-exposure surface of the catalysts. A concentration of ~ 700 ppm vaporous toluene, xylene or benzene in a gaseous mixture ($\text{N}_2/\text{O}_2 = 3:1$, relative humidity of $\sim 32.2\%$) and 0.2 g catalyst dispersed in a 7.0 cm^2 of quartz holder were used for each test. The VOCs conversions were calculated according to the CO_2 production and carbon balance [8]. The photothermocatalytic reduction of CO_2 by H_2O vapor was performed in a Pyrex reaction vessel with a volume of 43 mL coupled with a thermode and an ice bag. A Xe lamp ($\lambda = 420\text{--}780\text{ nm}$, 400 mW cm^{-2}) was used. The Pyrex reaction vessel was filled with CO_2 and H_2O vapor, and $\sim 6\text{ mg}$ catalyst was dispersed on the bottom of the Pyrex vessel for each test. The gaseous products were measured by gas chromatograph equipped with a flame ionization detector and a thermal conductive detector.

3. Results and discussion

3.1. Crystal structure, composition and morphology

The $\text{WO}_{3-x}\text{-R}/\text{GdCrO}_3$ was synthesized by a two-step procedure, namely, preparation of GdCrO_3 and hydrothermal growth of WO_{3-x} with rich defect sites (or $\text{WO}_{3-x}\text{-R}$) over GdCrO_3 (Fig. S2, Supporting Information). The tight $\text{WO}_{3-x}\text{-R}$ nanosheets with a length of $60 \pm 15\text{ nm}$ were mainly grown on the central surfaces of GdCrO_3 , which holds a dumbbell-like architecture with a length of $516 \pm 20\text{ nm}$ (Fig. S3a, Supporting Information), with a thickness of $\sim 23\text{ nm}$ (Fig. 1a-c). The $\text{WO}_{3-x}\text{-R}/\text{GdCrO}_3$ shows similar dumbbell-like morphology after the $\text{WO}_{3-x}\text{-R}$ growth (Fig. 1a and Fig. S3b, Supporting Information). EDS characterization of the dotted box region in Fig. 1a shows roughly a $\text{WO}_{3-x}\text{-R}$ to GdCrO_3 mole ratio of 3.04: 1 on the central surfaces of dumbbell-like $\text{WO}_{3-x}\text{-R}/\text{GdCrO}_3$ (Fig. S4 and Table S1, Supporting Information). The intimate contact between $\text{WO}_{3-x}\text{-R}$ and GdCrO_3 can be clearly observed on the HRTEM images that the WO_{3-x} nanosheets with rich defect sites robustly grow on GdCrO_3 with a $[-1, 0, 4]$ direction (Fig. 1b and c). The blueshift of the W-O stretching peak in the Raman

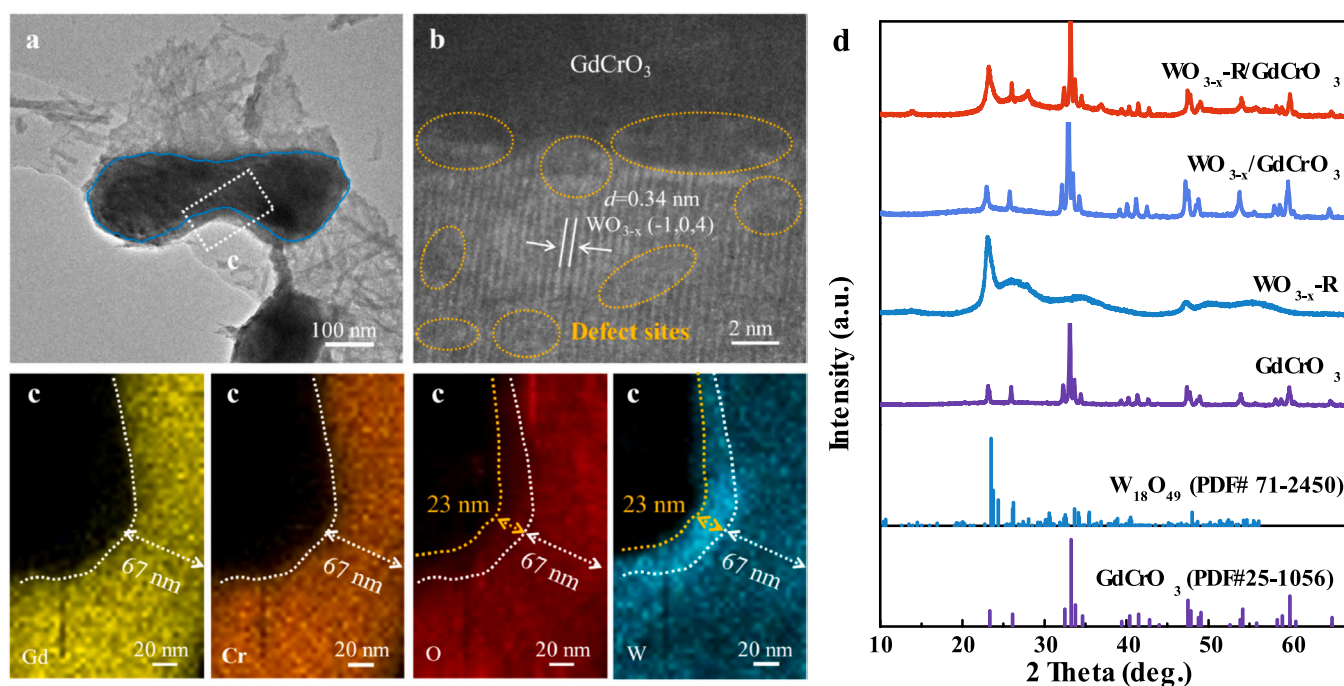


Fig. 1. (a) TEM, (b) HRTEM, and (c) elemental mapping images for the white dotted box area in (a) of $WO_{3-x-R}/GdCrO_3$, (d) XRD patterns of the samples.

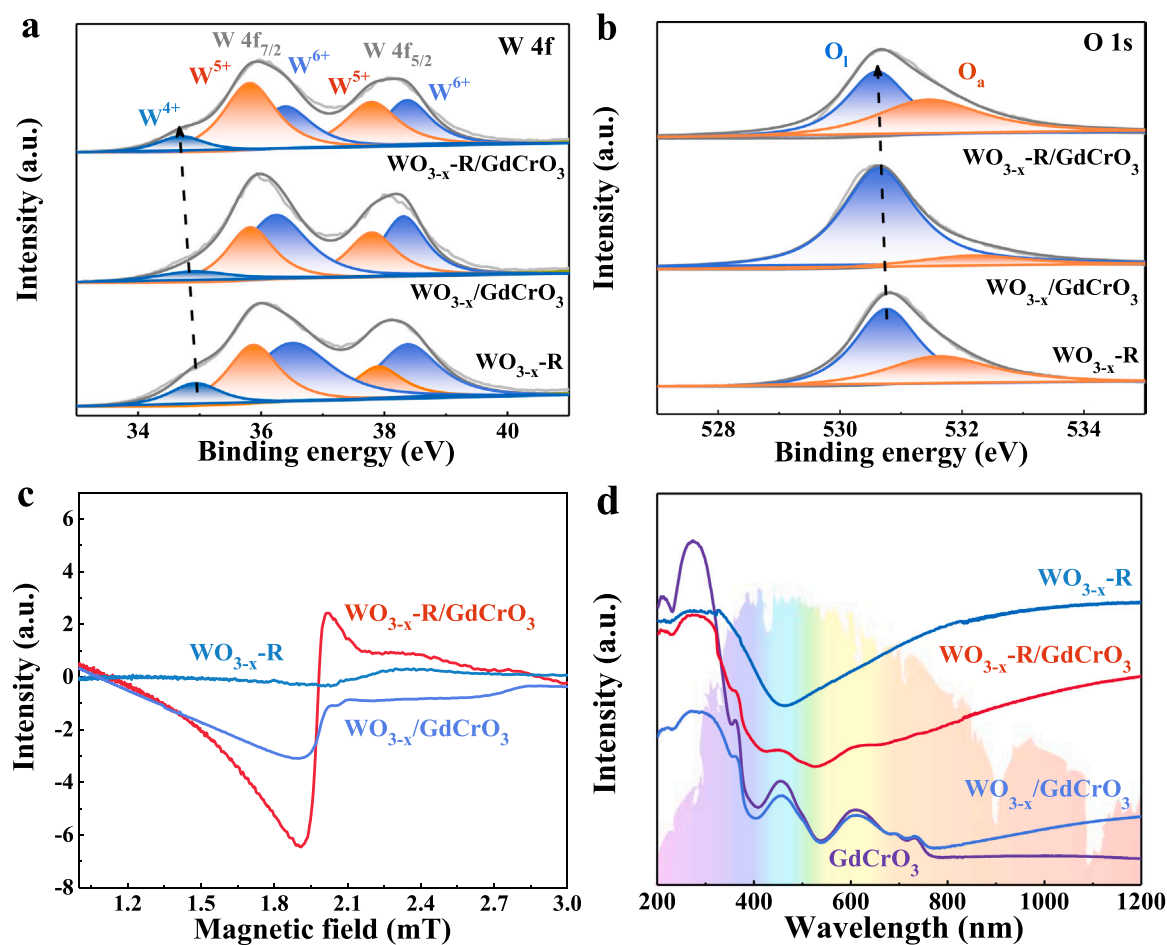
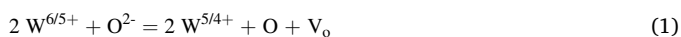


Fig. 2. (a) W 4f XPS spectra, (b) O 1s XPS spectra, (c) ESR spectra, and (d) UV-vis diffuse reflectance spectra of the samples.

spectra from 813 cm^{-1} for $\text{WO}_{3-x}\text{-R}$ to 797 cm^{-1} for $\text{WO}_{3-x}\text{-R}/\text{GdCrO}_3$ further reflects the strong interaction between $\text{WO}_{3-x}\text{-R}$ and GdCrO_3 (Fig. S5, Supporting Information). After the treatment of $\text{WO}_{3-x}\text{-R}/\text{GdCrO}_3$ in H_2O_2 solution, the obtained $\text{WO}_{3-x}/\text{GdCrO}_3$ keeps well the dumbbell-like morphology and tight $\text{WO}_{3-x}\text{-GdCrO}_3$ interfaces with the WO_{3-x} nanosheets grown on the GdCrO_3 core (Fig. S6a and b, Supporting Information). Both $\text{WO}_{3-x}/\text{GdCrO}_3$ and $\text{WO}_{3-x}\text{-R}/\text{GdCrO}_3$ are all composed by monoclinic $\text{W}_{18}\text{O}_{49}$ (PDF#71-2450) and orthorhombic GdCrO_3 (PDF#25-1056) (Fig. 1d). However, there is a significant decrease in the defect amount at WO_{3-x} surfaces and $\text{WO}_{3-x}\text{-GdCrO}_3$ interfaces after the treatment (Fig. S6c and d, Supporting Information).

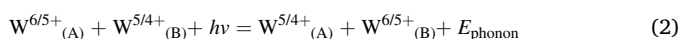
3.2. Electronic structures and optical properties

The W 4f XPS spectra of $\text{WO}_{3-x}\text{-R}$, $\text{WO}_{3-x}/\text{GdCrO}_3$, and $\text{WO}_{3-x}\text{-R}/\text{GdCrO}_3$ in Fig. 2a all show two main peaks of W 4f_{7/2} and W 4f_{5/2} at ~ 35.9 eV and ~ 38.1 eV, respectively, with a spin-orbit splitting of the doublet as ~ 2.2 eV, matching well with the previous reports [23,24]. All the W 4f spectra reveal the co-presences of W^{4+} with the characteristic peak at the binding energy (BE) of 34.7–34.9 eV, W^{5+} with the corresponding peaks at 35.6–35.9 and 37.8–37.9 eV, and W^{6+} with the related peaks at 36.2–36.5 and 38.3–38.4 eV (Fig. 2a, Table S2, Supporting Information) [22]. The presence of low valence states $\text{W}^{5/4+}$ in the samples is attributed to the loss of lattice O^{2-} to form oxygen vacancies along with the excessive electrons trapped by tungsten species, as described with Eq. 1 [22],



where O^{2-} , O, and V_O represent the lattice oxygen, free oxygen, and oxygen vacancy, respectively. The peaks of O 1s spectra in Fig. 2b at ~ 530.8 eV and ~ 531.6 eV are respectively related to lattice oxygen (O_l) and adsorbed oxygen species (O_a) at defect sites [22]. The interaction between $\text{WO}_{3-x}\text{-R}$ and GdCrO_3 leads to the blueshift of W^{4+} and O_l peaks in $\text{WO}_{3-x}\text{-R}/\text{GdCrO}_3$ in comparison with those in $\text{WO}_{3-x}\text{-R}$, indicating the electrons transfer at the interfaces through internal electric fields (IEF) [25]. Such an interaction or blueshift of W^{4+} and O_l peaks become weak in $\text{WO}_{3-x}/\text{GdCrO}_3$ with less defect sites at the interface, suggesting that the defect band state related IEF (DBIEF) is crucial for charge interaction in $\text{WO}_{3-x}\text{-R}/\text{GdCrO}_3$ interfaces (Fig. 2a and b). The relative amount of $\text{W}^{5/4+}$ species in these samples is evaluated according to the areas of their XPS peaks and holds the same sequence with the blueshift of W 4f peak, which shows larger oxygen vacancies amount along with the higher $\text{W}^{5/4+}$ species content in $\text{WO}_{3-x}\text{-R}/\text{GdCrO}_3$ in comparison with $\text{WO}_{3-x}/\text{GdCrO}_3$ and $\text{WO}_{3-x}\text{-R}$ (Table S2, Supporting Information). The ESR spectra were widely performed to analyze the contents of oxygen vacancies on catalysts [26,27]. As exhibited in Fig. 2c, the oxygen vacancy signal intensity of $\text{WO}_{3-x}\text{-R}/\text{GdCrO}_3$ is higher than those of $\text{WO}_{3-x}/\text{GdCrO}_3$ and $\text{WO}_{3-x}\text{-R}$ with g values at 1.977–2.145, further confirming its larger oxygen vacancies amount along with the higher $\text{W}^{5/4+}$ species content (Fig. 2c).

Both $\text{WO}_{3-x}\text{-R}$ and $\text{WO}_{3-x}\text{-R}/\text{GdCrO}_3$ with rich $\text{W}^{5/4+}$ defect sites hold full or near full visible light response, which are remarkably stronger than those of GdCrO_3 and $\text{WO}_{3-x}/\text{GdCrO}_3$ (Fig. 2d). Such an absorption promotion is ascribed to the LSPR response or collective oscillations of the excessive electrons on $\text{W}^{5/4+}$ defect sites (Fig. S7 and Table S3, Supporting Information), as described in Eq. 2 [28],



The bandgap values of WO_{3-x} (~ 2.76 eV), $\text{WO}_{3-x}\text{-R}$ (~ 2.66 eV) and GdCrO_3 (~ 2.37 eV), evaluated with the UV-vis spectra and a Kubelka-Munk method (Fig. S8a-c, Supporting Information) [8], also indicate their visible-light response ability. The n-type semiconductor character and conduction band (E_c) values of WO_{3-x} (~ 0.19 V), $\text{WO}_{3-x}\text{-R}$ (~ 0.19 V) and GdCrO_3 (~ -2.29 V) are proposed based on the active slopes and flat-band values from their Mot-Schottky (MS) plots

(Fig. S8d-f, Supporting Information) [29]. Accordingly, the valance band (E_v) values of WO_{3-x} (~ 2.95 V), $\text{WO}_{3-x}\text{-R}$ (~ 2.85 V), and GdCrO_3 (~ 0.08 V) are calculated. In addition, the Fermi level (E_f) positions of WO_{3-x} (~ 0.13 V), $\text{WO}_{3-x}\text{-R}$ (~ -0.43 V), and GdCrO_3 (~ -0.83 V) are estimated with their XPS valence spectra (Fig. S8d-f, Supporting Information). Moreover, the $\text{W}^{5/4+}$ defect-band state in XPS valence spectra of $\text{WO}_{3-x}\text{-R}$ suggests its defect-band bottom energy (E_DB) is 0.28 V. As schematically presented in Fig. 3a, both $\text{WO}_{3-x}/\text{GdCrO}_3$ and $\text{WO}_{3-x}\text{-R}/\text{GdCrO}_3$ hold the Type III heterojunction characteristic and bandgap-broken interfaces, and the enrichment of the $\text{W}^{5/4+}$ defects reduce the barrier gap to some extent due to the negative E_f shift in $\text{WO}_{3-x}\text{-R}$.

The band structures of WO_{3-x} , $\text{WO}_{3-x}\text{-R}$, and GdCrO_3 were further studied by the density of states (DOS) calculations (Fig. 3b and c, Fig. S9 and S10a, Supporting Information), giving respectively the similar bandgap values of 2.63 eV, 2.56 eV, and 2.39 eV with above-evaluated values by experiments. The larger bandgap of WO_{3-x} than that of defect-enriched $\text{WO}_{3-x}\text{-R}$ measured by experiment is also revealed by the calculated band structures (Fig. 3b and c). Partial DOS (PDOS) analysis suggests the E_v orbits of WO_{3-x} , $\text{WO}_{3-x}\text{-R}$, and GdCrO_3 are composed of O 2p, and their E_c bottoms are respectively contributed by W 5d_g, W 5d_g, and Cr 3d_z²/Cr 3d_{xz} orbits (Fig. 3d and Fig. S10b and c, Supporting Information). There is a single and independent E_DB peak at W 5d_g/O 2p hybrid orbits between the E_c and E_v orbits of WO_{3-x} (Fig. S10c, Supporting Information). After introducing the oxygen defects, the E_DB range at hybrid orbits of W 5d/O 2p_y + 2p_z in $\text{WO}_{3-x}\text{-R}$ is enlarged comparing to that of WO_{3-x} and even surpass the energy level of E_c (Fig. 3d, Fig. S9a and b, Supporting Information). Thus, the photo-generated electrons of $\text{WO}_{3-x}\text{-R}$ can be partially captured by the $\text{W}^{5/4+}$ defect sites, at the same time, the captured electrons at the defect band can be excited again due to their LSPR effect (Fig. S11, supporting information), making a possibility of a continued transitions of excessive electrons from E_f at hybrid orbits of W 5d_g/O 2p_y + 2p_z to the higher energy levels under light irradiation (Fig. 3d).

3.3. Defect band bridge for charges transfer

Fig. 4a compares the photocurrent intensity of the samples. At 298 K, the $\text{WO}_{3-x}\text{-R}/\text{GdCrO}_3$ shows comparable photocurrent intensity with the component $\text{WO}_{3-x}\text{-R}$, indicating the negligible promotion of the heterojunction formation on the generation and separation of the photoinduced charges. Upon raising the temperature to 333 K, the $\text{WO}_{3-x}\text{-R}/\text{GdCrO}_3$ exhibits remarkably higher photocurrent intensity than both $\text{WO}_{3-x}\text{-R}$ and GdCrO_3 , which can be attributed to the enhanced charges separation in consideration with the stronger light absorption ability of $\text{WO}_{3-x}\text{-R}$ (Fig. 2d). However, such a promotion effect of temperature is not observed on $\text{WO}_{3-x}/\text{GdCrO}_3$ with less $\text{W}^{5/4+}$ defect sites at the interface.

Under photothermal conditions, both the energy and concentration of LSPR induced hot electrons at the defect-rich $\text{WO}_{3-x}\text{-R}/\text{GdCrO}_3$ interface are enhanced (Fig. S11, Supporting Information). The energetic hot electrons may overcome the energy barrier at the interface and open a photothermal synergistic channel for charges transfer. The negative shift of the flat band potential (E_fb) from 0.29 V for WO_{3-x} to -0.23 V for $\text{WO}_{3-x}\text{-R}$ at 298 K indicates the promotion effect of $\text{W}^{5/4+}$ defect sites for enlarging the charge distribution range and tailoring the band bending in WO_{3-x} (Fig. S12, Supporting Information). Accordingly, $\text{WO}_{3-x}\text{-R}/\text{GdCrO}_3$ shows a more negative E_fb value of -0.33 V than that of $\text{WO}_{3-x}/\text{GdCrO}_3$ with limited $\text{W}^{5/4+}$ defect sites (~ -0.07 V) at 298 K after the heterojunction formation with GdCrO_3 (Fig. 4b&c). Upon raising the temperature to 333 K, a small negative shift of E_fb to -0.14 V is checked for $\text{WO}_{3-x}/\text{GdCrO}_3$, while it is as large as to -0.93 V for $\text{WO}_{3-x}\text{-R}/\text{GdCrO}_3$, which is even more negative than the Fermi level of GdCrO_3 (-0.83 V) (Fig. 3a and Fig. 4c). These results convince that the introduction of efficient $\text{W}^{5/4+}$ defect sites makes it possible to excite the hot electrons from the Fermi level of $\text{WO}_{3-x}\text{-R}$ to a

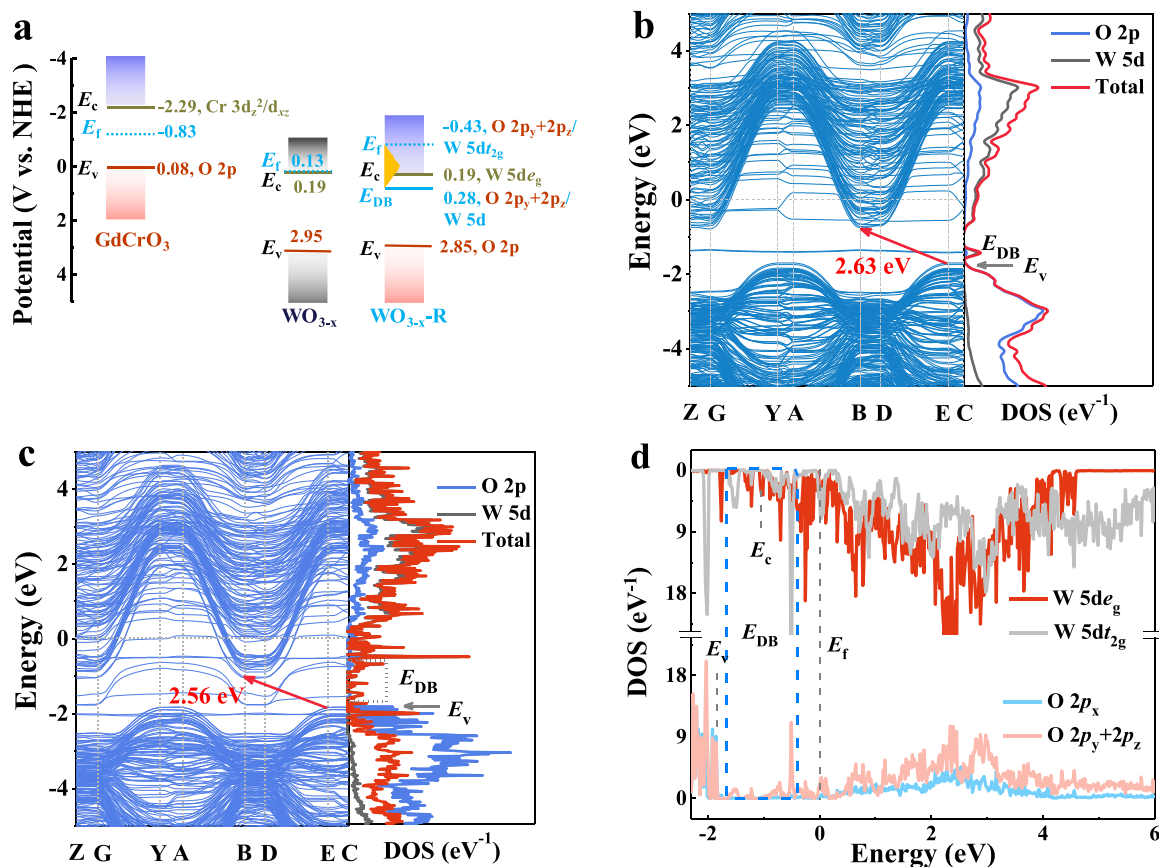


Fig. 3. (a) Band structure scheme of the semiconductors, (b & c) Band structures and density of states (DOS) of WO_{3-x} and WO_{3-x-R}, and (d) Partial DOS (PDOS) of O 2p and W 5d orbitals of WO_{3-x-R}.

higher energy level for recombining the photoinduced holes at the valence band of GdCrO₃ under certain photothermal conditions.

Theoretical FDTD simulation was employed to further understand the charges transfer process at the interfaces of defect-rich WO_{3-x-R}/GdCrO₃. The WO_{3-x-R}/GdCrO₃ was modeled with a simple dumbbell-like structure according to its SEM and TEM images (inset in Fig. 4d). When the temperature 298 K and excited wavelength of 480 nm are employed, at which the defect-related LSPR effect is weak (Fig. 2d), the electric field enhanced factor (E^2/E_0^2), which reveals the concentration of the charges [10], at the WO_{3-x-R}/GdCrO₃ interface (~ 1.6) is larger than that on the bulk WO_{3-x-R} (~ 1.3) (Fig. 4d). In other words, the enrichment of photoinduced charges at the interfaces happens due to the restricted interphase charges transfer and recombination at the gap-broken interface. As a comparison, the E^2/E_0^2 value at the WO_{3-x-R}/GdCrO₃ interface is obviously smaller than those on the bulk WO_{3-x-R} and GdCrO₃ for the excitation wavelength of 600 nm with a strong defect-related LSPR effect (Fig. 4e&f), indicating efficient charges transfer and recombination at the interface. Particularly, the E^2/E_0^2 values of WO_{3-x-R} and GdCrO₃ components are significantly enhanced under photothermal condition at 333 K (Fig. 4f), which is attributed to the enhanced light absorption and photoinduced charges separation through the selective recombination of the electrons from WO_{3-x-R} and holes on GdCrO₃ at the interfaces assisted by the defect-related LSPR.

The ultrafast transient absorption (TA) kinetic curves of WO_{3-x-R}, WO_{3-x}/GdCrO₃, and WO_{3-x-R}/GdCrO₃ in Fig. 4g measured at 333 K all show two TA signals. The first one at 0.06–0.21 ps is ascribed to the relaxation of the hot electrons, and another one with a slow decay process around 0.20–0.43 ps relates to the photothermal effect caused by the LSPR excitation of the hot electrons at the W^{5/4+} defect states [10]. As compared, the WO_{3-x-R}/GdCrO₃ heterostructure exhibits a faster LSPR signal decay or hot electrons relaxation time (~ 0.06 ps) than

that on WO_{3-x-R} (~ 0.13 ps). Similar phenomenon was reported on the heterostructure W₁₈O₄₉/TiO₂, which was attributed to the ultrafast transfer of the hot electrons from the W₁₈O₄₉ to TiO₂ [10]. In contrast, the first TA signal of WO_{3-x}/GdCrO₃ without efficient interfacial W^{5/4+} defect sites and hot electrons to overcome energy barrier of gap-broken heterojunction prolongs to 0.21 ps. The TA decay curves of the samples at various probe wavelengths of 560–640 nm were also measured and fitted by the exponential decay functions to further analyze the hot electrons transfer kinetics. The TA decay curves of WO_{3-x-R} and WO_{3-x}/GdCrO₃ were well fitted by the triexponential function (Fig. S13 & S14, Supporting Information), giving three time constants τ_1 , τ_2 , and τ_3 , which represent the relaxation of hot electron from excited state to middle energy state [10,30–32], the decay time from middle energy state to the ground state [10], and the recombination time at W^{5/4+} defect states, respectively. The regressed τ_1 , τ_2 , and τ_3 values of WO_{3-x-R} are 0.17–4.35 ps, 7.90–21.30 ps and 3.30–47.20 ps, and they are 10.2–33.1 ps, 0.14–2.04 ps and 0.14–6.12 ps for WO_{3-x}/GdCrO₃. As a comparison, the TA curves of WO_{3-x-R}/GdCrO₃ obey the mono-exponential function, only providing a short decay time τ_1 from excited state to middle energy state as 0.08–1.34 ps (Fig. S15, Supporting Information), further proving the rapid hot carriers transfer from WO_{3-x-R} to GdCrO₃. The average decay time (τ_{ave}) of the materials was also calculated (Fig. S13–S15, Supporting Information). As expected, the τ_{ave} of WO_{3-x-R}/GdCrO₃ (0.08–1.34 ps) is remarkably shorter than those of WO_{3-x-R} (3.3–43.9 ps) and WO_{3-x}/GdCrO₃ (8.3–17.3 ps) (Fig. 4h).

The carriers recombination rates (k_{cr}) at the WO_{3-x-R}-GdCrO₃ interfaces was then evaluated by the following Eq. 3 [10].

$$k_{cr} = 1/\tau_{ave}(\text{WO}_{3-x-R}/\text{GdCrO}_3) - 1/\tau_{ave}(\text{WO}_{3-x-R}) \quad (3)$$

The high charges transfer and recombination efficiency at the

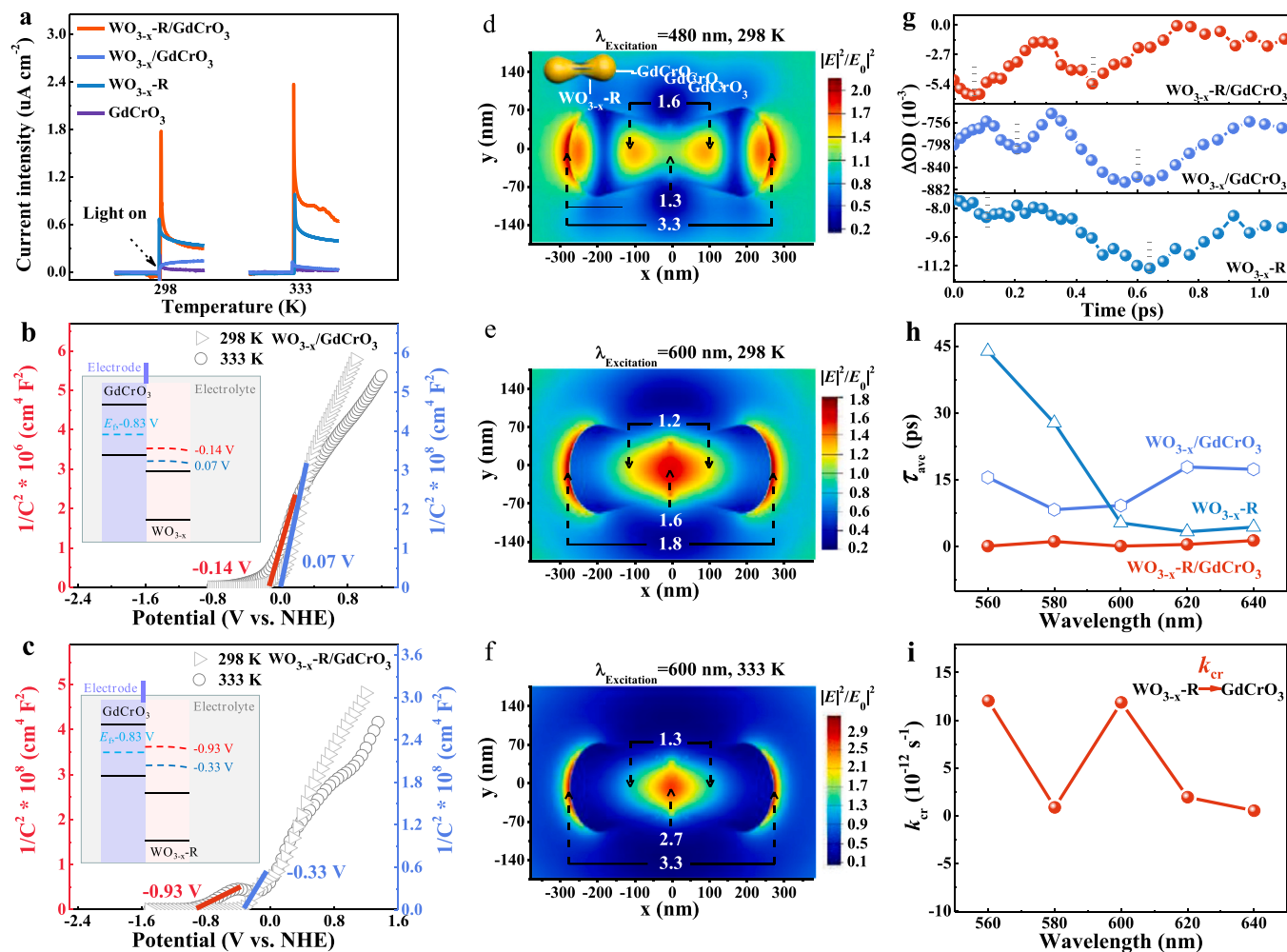


Fig. 4. (a) Photocurrent curves and (b&c) Mott-Schottky (M-S) plots of the samples at various temperatures. Insets in b&c are the corresponding schematic band bending diagrams. (d-f) FDTD simulation of $\text{WO}_{3-x}\text{-R}/\text{GdCrO}_3$ with irradiation wavelengths: (d) 480 nm and (e) 600 nm at 298 K, and (f) 600 nm at 333 K. Inset in (d) is the $\text{WO}_{3-x}\text{-R}/\text{GdCrO}_3$ mode for calculation. (g) Transient absorption (TA) kinetics curves with irradiation wavelength of 600 nm, (h) Average decay time at various probing wavelengths of the samples at 333 K. (i) Charge transfer rate constants at $\text{WO}_{3-x}\text{-R}/\text{GdCrO}_3$ interfaces at various probing wavelengths at 333 K.

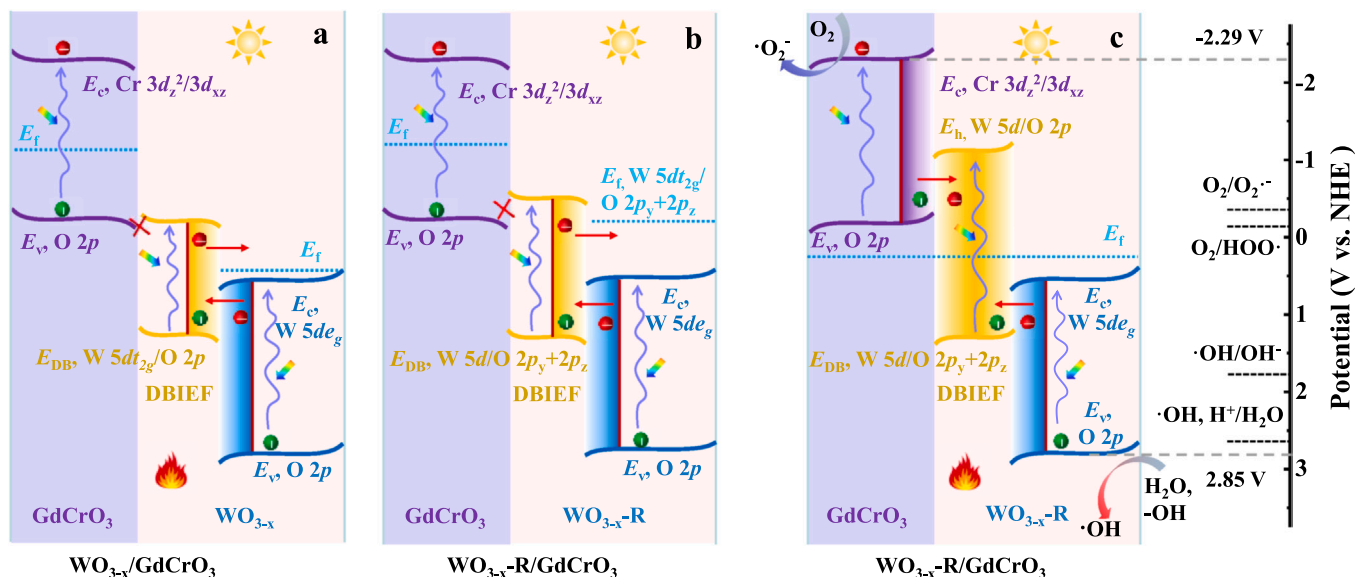


Fig. 5. Schematic diagram of charges migration and separation in heterojunctions: (a) $\text{WO}_{3-x}/\text{GdCrO}_3$ at photothermal condition, (b&c) $\text{WO}_{3-x}\text{-R}/\text{GdCrO}_3$ at a single photoexcited or photothermal condition. DBIEF represents the defect band internal electric fields (or defect band bridge) at the interfaces.

$\text{WO}_{3-x}\text{-R-GdCrO}_3$ interfaces with the k_{cr} as fast as $5.20 \times 10^{11} \sim 1.20 \times 10^{13} \text{ s}^{-1}$ at various excitation wavelength light and 333 K is revealed (Fig. 4i), which explains well the short hot electrons decay time from the excited state to middle energy state and undetectable electrons decay signals from middle energy state to the ground state or the recombination at the defective states of $\text{WO}_{3-x}\text{-R/GdCrO}_3$. As compared, the strong LSPR intensity accompanies with fast interfacial charges transfer kinetics.

Accordingly, the transfer and selective recombination of the photo-induced charges in the $\text{WO}_{3-x}\text{/GdCrO}_3$ and $\text{WO}_{3-x}\text{-R/GdCrO}_3$ heterojunctions is proposed and illustrated in Fig. 5. Upon visible light irradiation, WO_{3-x} , $\text{WO}_{3-x}\text{-R}$ and GdCrO_3 in $\text{WO}_{3-x}\text{/GdCrO}_3$ and $\text{WO}_{3-x}\text{-R/GdCrO}_3$ can be excited for generating photoexcited holes in valance orbits O 2p and electrons in conduction band (CB) orbits W 5 d_{eg} , W 5 d_{eg} and Cr 3 d_{z^2} /Cr 3 d_{xz} , respectively. The $\text{W}^{5/4+}$ (or oxygen vacancies) defects in $\text{WO}_{3-x}\text{-R}$ introduce the defect band (DB, E_{DB}) composed by the hybrid orbits of W 5d/O 2p_y + 2p_z with a range to cover its E_{c} and approach to its E_{v} and E_{f} (Fig. 3d). Thus, the photogenerated electrons of $\text{WO}_{3-x}\text{-R}$ can be partially captured by the $\text{W}^{5/4+}$ defect sites, at the same time, the captured electrons at the defect band can be excited again due to their LSPR effect (Fig. 2d & Fig. S11, Supporting Information) [10]. Under certain photothermal conditions, e.g., 333 K & visible light irradiation, the excited hot electrons can continuously transfer across the $\text{WO}_{3-x}\text{-R-GdCrO}_3$ interfaces for overcoming the broken energy barrier in $\text{WO}_{3-x}\text{-R/GdCrO}_3$ and recombining with the photogenerated holes at the VB of GdCrO_3 (Fig. 5c). The negative shift of the flat band potential (E_{fb}) from 0.29 V for WO_{3-x} to -0.23 V for $\text{WO}_{3-x}\text{-R}$ at 298 K indicates the promotion effect of $\text{W}^{5/4+}$ defect sites

for enlarging the charge distribution range and tailoring the band bending in WO_{3-x} (Fig. S12, Supporting Information). The E_{fb} of $\text{WO}_{3-x}\text{-R/GdCrO}_3$ at 333 K shifts negatively as large as to -0.93 V, which is even more negative than the Fermi level of GdCrO_3 (-0.83 V) (Fig. 3a and Fig. 4c), convincing that the introduction of efficient $\text{W}^{5/4+}$ defect sites makes it possible to excite the hot electrons from the Fermi level of $\text{WO}_{3-x}\text{-R}$ to a higher energy level for recombining the photo-induced holes at the VB of GdCrO_3 under certain photothermal conditions. In addition, the FDTD simulation (Fig. 4f) and fast interfacial charges transfer rate measured by transient absorption (Fig. 4i) also support such transfer mode. As a reference and comparison, the limited interfacial defect sites with insufficient trapped electrons and weak LSPR response leads to a small negative shift of E_{fb} to -0.14 V in $\text{WO}_{3-x}\text{/GdCrO}_3$ at 333 K. Meanwhile, the insufficient photothermal conditions at 298 K also results in a small negative E_{fb} value of -0.33 V in $\text{WO}_{3-x}\text{-R/GdCrO}_3$. Both cases are difficult to sustainably excite the hot electrons to an energy level higher than that of E_{f} (-0.83 V) for GdCrO_3 (Fig. 5a&b). In short, the defect band $\text{W}^{5/4+}$ bridge activates the gap-broken Type III $\text{WO}_{3-x}\text{/GdCrO}_3$ heterojunction through a photothermal plasmonic resonance assisted transfer process at the $\text{WO}_{3-x}\text{-R-GdCrO}_3$ interfaces, endowing a robust defect-band bridged (or Type B) $\text{WO}_{3-x}\text{-R/GdCrO}_3$ heterojunction with full visible-light response range and efficient separation of photoinduced charges with a preservation of the electrons/holes with strong redox ability for the catalytic redox reactions.

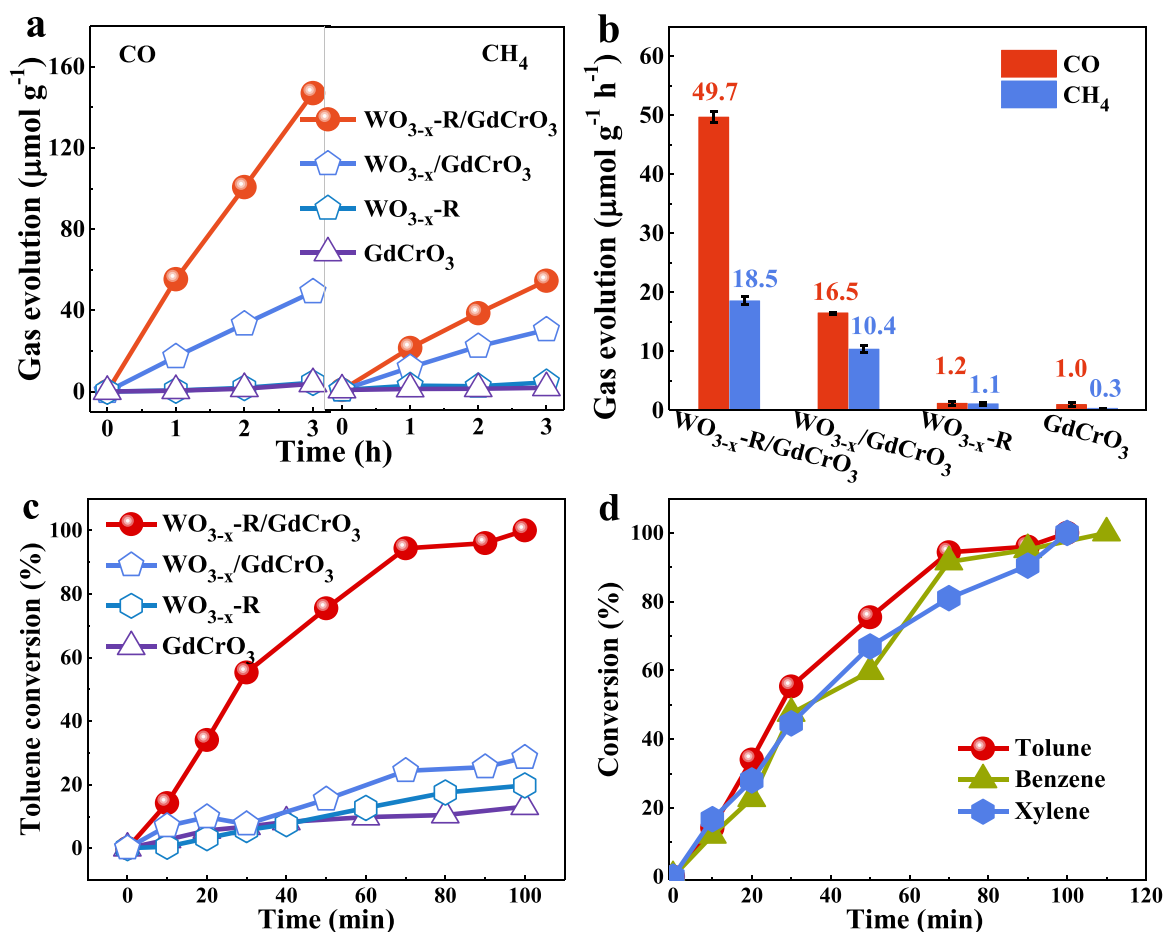
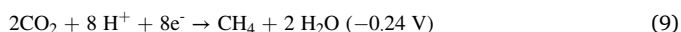
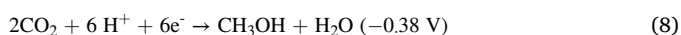
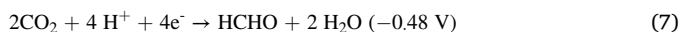
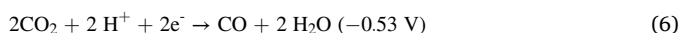
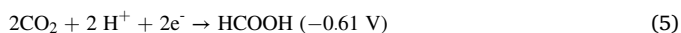
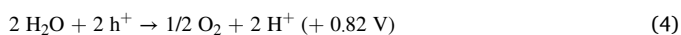


Fig. 6. (a) CO and CH₄ production curves and (b) CO & CH₄ yield rates from photothermocatalytic (PTC) CO₂ reduction (light: 420 nm~780 nm, 333 K). (c) Performance comparison of photothermocatalytic (PTC, 420~780 nm, 333 K) toluene degradation. (d) PTC toluene, benzene, and xylene degradation by $\text{WO}_{3-x}\text{-R/GdCrO}_3$.

3.4. Photothermocatalytic performance

The photothermocatalytic or photocatalytic performance of the heterojunctions usually shows positive correlation to the production ability of $\bullet\text{OH}$ and $\bullet\text{O}_2^-$ [33–35]. As expected, the $\text{WO}_{3-x}\text{-R}/\text{GdCrO}_3$ shows remarkable higher $\bullet\text{OH}$ and $\bullet\text{O}_2^-$ production ability than the reference samples $\text{WO}_{3-x}/\text{GdCrO}_3$, WO_{3-x} and GdCrO_3 after visible light irradiating for 5 min (Fig. S16a and b, Supporting Information) due to its enhanced light absorption and photoinduced charges separation, although the irradiation induced temperature rise of $\text{WO}_{3-x}\text{-R}/\text{GdCrO}_3$ (~ 353.1 K) is lower than that of WO_{3-x} (~ 371.0 K) (Fig. S16c&d, Supporting Information). The photothermocatalytic CO_2 reduction and VOCs degradation reactions were explored as the model reactions to further evaluate the application potentials of Type B heterojunction $\text{WO}_{3-x}\text{-R}/\text{GdCrO}_3$ in energy and environmental catalysis fields. As compared in Fig. 6 a and b, the photothermocatalytic (PTC, 420 nm–780 nm, 333 K) CO and CH_4 yielding rates by CO_2 reduction over $\text{WO}_{3-x}\text{-R}/\text{GdCrO}_3$ are as high as $49.6 \mu\text{mol g}^{-1} \text{h}^{-1}$ (CO) and $18.5 \mu\text{mol g}^{-1} \text{h}^{-1}$ (CH_4), which are thrice & twice, 42 & 17 times, and 50 & 54 times higher than those of $\text{WO}_{3-x}/\text{GdCrO}_3$, $\text{WO}_{3-x}\text{-R}$, and GdCrO_3 , respectively, even though the BET surface area of $\text{WO}_{3-x}\text{-R}/\text{GdCrO}_3$ ($36 \text{ m}^2 \text{g}^{-1}$) is greatly smaller than that of $\text{WO}_{3-x}\text{-R}$ ($82 \text{ m}^2 \text{g}^{-1}$). The photothermocatalytic CO_2 reduction. The photothermocatalytic CO_2 reduction process in the solid-gas reactive system without adding the other sacrificial agents can be illustrated with Eqs. 4 and 9 by referring the previous reports [36–40]. In consideration with that the energy barrier of CO_2 reduction to produce CH_4 is lower than those of HCHO , HCOOH , and CH_3OH , etc, and the production of CO needs less electrons [36–40], except for CO_2 , O_2 , CO and CH_4 , herein, the other carbon-involved species are all below the detection limit of the gas chromatography.



The photothermocatalytic CO_2 reduction to value-added products without additional sacrificial agent and noble metal catalysts is more desired but with larger challenge. In this work, the as-developed Type B heterojunction $\text{WO}_{3-x}\text{-R}/\text{GdCrO}_3$ shows great application potential for such a process, holding obviously higher CO& CH_4 production rates of $\text{WO}_{3-x}\text{-R}/\text{GdCrO}_3$ from photothermocatalytic CO_2 reduction than most of the recently reported materials and CO_2 reduction process without adding the sacrificial agent and noble-metal cocatalysts (Table S4, Supporting Information). Notably, the CH_4 yielding rates from catalytic CO_2 reduction of non-noble metal $\text{WO}_{3-x}\text{-R}/\text{GdCrO}_3$ ($18.5 \mu\text{mol g}^{-1} \text{h}^{-1}$) at 333 K is even higher than that of $9.6 \mu\text{mol g}^{-1} \text{h}^{-1}$ for $\text{WO}_3/\text{Ag}/\text{GdCrO}_3$ containing noble metal Ag at a higher reaction temperature of 363 K [9]. In addition, the $\text{WO}_{3-x}\text{-R}/\text{GdCrO}_3$ holds well cyclic stability for PTC CO_2 reduction (Fig. S17a, Supporting Information). As aforementioned, only under certain photothermal condition, the Type B $\text{WO}_{3-x}\text{-R}/\text{GdCrO}_3$ can be activated as a robust catalyst. The $\text{WO}_{3-x}\text{-R}/\text{GdCrO}_3$ shows poor photocatalytic CO_2 reduction activity under single visible light irradiation condition with low CO and CH_4 yielding rates of $14.0 \mu\text{mol g}^{-1} \text{h}^{-1}$ and $9.7 \mu\text{mol g}^{-1} \text{h}^{-1}$ and negligible thermocatalytic CO_2 reduction activity (Fig. S17b, Supporting Information).

The applicability of the Type B heterojunction $\text{WO}_{3-x}\text{-R}/\text{GdCrO}_3$ was further checked for photothermocatalytic (PTC) toluene degradation. Almost 100% toluene degradation with an initial ~ 700 ppm toluene and

relative humidity (RH) of 32% is achieved by PTC oxidation over $\text{WO}_{3-x}\text{-R}/\text{GdCrO}_3$ at 333 K under visible light irradiation (420–780 nm) within 100 min (Fig. 6c). The PTC toluene degradation rate of $\text{WO}_{3-x}\text{-R}/\text{GdCrO}_3$ is 5–14 times higher than that of $\text{WO}_{3-x}/\text{GdCrO}_3$, WO_{3-x} , and GdCrO_3 (Fig. S18a, Supporting Information), and better than those of the recent photocatalytic or PTC materials (Table S5, Supporting Information). The $\text{WO}_{3-x}\text{-R}/\text{GdCrO}_3$ also shows good stability for cyclic PTC toluene degradation (Fig. S18b, Supporting Information). The influence of reaction temperature on the photothermocatalytic activity of the as-developed $\text{WO}_{3-x}\text{-R}/\text{GdCrO}_3$ was also evaluated (Fig. S18c and d, Supporting Information). The photothermocatalytic toluene degradation rate constants increase from 0.029 min^{-1} to 0.13 min^{-1} upon raising the reaction temperature from 333 K to 393 K. The effect of the $\text{WO}_{3-x}\text{-R}/\text{GdCrO}_3$ composition on the photothermocatalytic performance was also tested (Fig. S19, Supporting Information), demonstrating that the as-developed $\text{WO}_{3-x}\text{-R}/\text{GdCrO}_3$ holds suitable composition and components interaction as an efficient photothermal catalyst. Moreover, the type B heterojunction $\text{WO}_{3-x}\text{-R}/\text{GdCrO}_3$ shows excellent performance for PTC degradation of xylene and benzene decomposition (Fig. 6d). Therefore, the Type B heterojunction $\text{WO}_{3-x}\text{-R}/\text{GdCrO}_3$ possesses enormous potential as robust photothermocatalytic materials for energy and environmental applications.

4. Conclusions

Type III heterojunction $\text{WO}_{3-x}/\text{GdCrO}_3$ was activated as a robust Type B heterojunction $\text{WO}_{3-x}\text{-R}/\text{GdCrO}_3$ photothermocatalyst through introducing $\text{W}^{5+/4+}$ defect sites at the interfaces and making use of the defect band as the bridge for storage, secondary plasmonic excitation, and interband transfer of the photothermal induced charges. In this way, efficient charge separation, high redox potential, and full visible light absorption were achieved. The Type B heterojunction $\text{WO}_{3-x}\text{-R}/\text{GdCrO}_3$ demonstrated excellent photothermocatalytic performance in CO_2 reduction with high CO and CH_4 yielding rates of $49.6 \mu\text{mol g}^{-1} \text{h}^{-1}$ and $18.5 \mu\text{mol g}^{-1} \text{h}^{-1}$ in gas-solid reaction system without sacrifice agent, as well as in VOCs degradation, evidently ranging among the best of those reported in the literature. This work paves a new path in refreshing the application potentials of bandgap broken Type III heterojunctions or designing efficient heterojunction catalysts for solar-light driven systems.

CRedit authorship contribution statement

Jingwei Li: Investigation, Formal analysis, Data curation, Methodology, Writing – original draft. **Jianrui Feng:** DFT calculations, Writing – review & editing. **Xiaomin Guo:** CO_2 reduction tests and discussion. **Hongli Fang:** Characterization and discussion. **Jiayi Chen:** VOCs oxidation tests and discussion. **Churong Ma:** FDTD calculations, Writing – review & editing. **Ruchun Li:** Discussion, Writing – review & editing. **Yuya Wang:** Discussion on FDTD calculations. **Zebao Rui:** Conceptualization, Methodology, Formal analysis, Resources, Supervision, Data curation, Funding acquisition, Writing – review & editing.

Declaration of Competing Interest

The authors declare that they have no known competing financial interests or personal relationships that could have appeared to influence the work reported in this paper.

Acknowledgements

This work was supported by the National Natural Science Foundation of China (21776322), Natural Science Foundation for Distinguished Young Scholars of Guangdong Province, China, and Guangdong Province Science and Technology Innovation Strategy Special Fund project (pdjh2020a0006). The contribution from Dr. Ruqian Lian at Jilin

University for the DFT calculation and discussion, as well as Dr. Cong Wang at Paris-Sud University for the helpful discussion is appreciated.

Appendix A. Supporting information

Supplementary data associated with this article can be found in the online version at [doi:10.1016/j.apcatb.2022.121248](https://doi.org/10.1016/j.apcatb.2022.121248).

References

- [1] W. Hou, S.B. Cronin, A review of surface plasmon resonance-enhanced photocatalysis, *Adv. Funct. Mater.* 23 (2013) 1612–1619.
- [2] Z.-J. Wang, H. Song, H. Liu, J. Ye, Coupling of solar energy and thermal energy for carbon dioxide reduction: status and prospects, *Angew. Chem. Int. Ed.* 59 (2020) 8016–8035.
- [3] R. Marschall, Semiconductor composites: strategies for enhancing charge carrier separation to improve photocatalytic activity, *Adv. Funct. Mater.* 24 (2014) 2421–2440.
- [4] J. Low, J. Yu, M. Jaroniec, S. Wageh, A.A. Al-Ghamdi, Heterojunction photocatalysts, *Adv. Mater.* 29 (2017), 1601694.
- [5] S. Bai, J. Jiang, Q. Zhang, Y. Xiong, Steering charge kinetics in photocatalysis: intersection of materials syntheses, characterization techniques and theoretical simulations, *Chem. Soc. Rev.* 44 (2015) 2893–2939.
- [6] Q. Xu, L. Zhang, B. Cheng, J. Fan, J. Yu, S-scheme heterojunction photocatalyst, *Chem* 6 (2020) 1543–1559.
- [7] L. Su, L. Luo, H. Song, Z. Wu, W. Tu, Z.-J. Wang, J. Ye, Hemispherical shell-thin lamellar WS₂ porous structures composited with CdS photocatalysts for enhanced H₂ evolution, *Chem. Eng. J.* 388 (2020), 124346.
- [8] J. Li, X. Yang, C. Ma, Y. Lei, Z. Cheng, Z. Rui, Selectively recombining the photoinduced charges in bandgap-broken Ag₃PO₄/GdCrO₃ with a plasmonic Ag bridge for efficient photothermocatalytic VOCs degradation and CO₂ reduction, *Appl. Catal. B. Environ.* 291 (2021), 120053.
- [9] J. Li, J. Chen, H. Fang, X. Guo, Z. Rui, Plasmonic metal bridge leading type III heterojunctions to robust type B photothermocatalysts, *Ind. Eng. Chem. Res.* 60 (2021) 8420–8429.
- [10] Z. Zhang, X. Jiang, B. Liu, L. Guo, N. Lu, L. Wang, J. Huang, K. Liu, B. Dong, IR-driven ultrafast transfer of plasmonic hot electrons in nonmetallic branched heterostructures for enhanced H₂ generation, *Adv. Mater.* 30 (2018), 1705221.
- [11] H. Cheng, T. Kamegawa, K. Mori, H. Yamashita, Surfactant-free nonaqueous synthesis of plasmonic molybdenum oxide nanosheets with enhanced catalytic activity for hydrogen generation from ammonia borane under visible light, *Angew. Chem. Int. Ed.* 53 (2014) 2910–2914.
- [12] I. Kriegl, C. Jiang, J. Rodriguez-Fernandez, R.D. Schaller, D.V. Talapin, E. D. Como, J. Feldmann, Tuning the excitonic and plasmonic properties of copper chalcogenide nanocrystals, *J. Am. Chem. Soc.* 134 (2012) 1583–1590.
- [13] Y. Zhang, S. He, W. Guo, Y. Hu, J. Huang, J.R. Mulcahy, W.D. Wei, Surface-plasmon-driven hot electron photochemistry, *Chem. Rev.* 118 (2018) 2927–2954.
- [14] Z.-J. Wang, H. Song, H. Pang, Y. Ning, T.D. Dao, Z. Wang, H. Chen, Y. Weng, Q. Fu, T. Nagao, Y. Fang, J. Ye, Photo-assisted methanol synthesis via CO₂ reduction under ambient pressure over plasmonic Cu/ZnO catalysts, *Appl. Catal. B. Environ.* 250 (2019) 10–16.
- [15] H. Song, X. Meng, Z.-J. Wang, H. Liu, J. Ye, Solar-energy-mediated methane conversion, *Joule* 3 (2019) 1606–1636.
- [16] Z. Zhang, J. Huang, Y. Fang, M. Zhang, K. Liu, B. Dong, A nonmetal plasmonic Z-scheme photocatalyst with UV- to NIR-driven photocatalytic protons reduction, *Adv. Mater.* 29 (2017), 1606688.
- [17] Z. Lou, Q. Gu, L. Xu, Y. Liao, C. Xue, Surfactant-free synthesis of plasmonic tungsten oxide nanowires with visible-light-enhanced hydrogen generation from ammonia borane, *Chem. Asian J.* 10 (2015) 1291–1294.
- [18] C. Feng, L. Tang, Y. Deng, J. Wang, Y. Liu, X. Ouyang, Z. Chen, H. Yang, J. Yu, J. Wang, Maintaining stable LSPR performance of W₁₈O₄₉ by protecting its oxygen vacancy: a novel strategy for achieving durable sunlight driven photocatalysis, *Appl. Catal. B. Environ.* 276 (2020), 119167.
- [19] H. Zhang, Y. Wang, S. Zuo, W. Zhou, J. Zhang, X.W.D. Lou, Isolated cobalt centers on W₁₈O₄₉ nanowires perform as a reaction switch for efficient CO₂ photoreduction, *J. Am. Chem. Soc.* 143 (2021) 2173–2177.
- [20] C. Feng, L. Tang, Y. Deng, J. Wang, W. Tang, Y. Liu, Z. Chen, J. Yu, J. Wang, Q. Liang, Synthesis of branched WO₃@W₁₈O₄₉ homojunction with enhanced interfacial charge separation and full-spectrum photocatalytic performance, *Chem. Eng. J.* 389 (2020), 124474.
- [21] G. Xi, S. Ouyang, P. Li, J. Ye, Q. Ma, N. Su, H. Bai, C. Wang, Ultrathin W₁₈O₄₉ nanowires with diameters below 1 nm: synthesis, near-infrared absorption, photoluminescence, and photochemical reduction of carbon dioxide, *Angew. Chem. Int. Ed.* 51 (2012) 2395–2399.
- [22] N. Zhang, A. Jalil, D. Wu, S. Chen, Y. Liu, C. Gao, W. Ye, Z. Qi, H. Ju, C. Wang, X. Wu, L. Song, J. Zhu, Y. Xiong, Refining defect states in W₁₈O₄₉ by Mo doping: a strategy for tuning N₂ activation towards solar-driven nitrogen fixation, *J. Am. Chem. Soc.* 140 (2018) 9434–9443.
- [23] A. Romanyuk, P. Oelhofen, Evidence of different oxygen states during thermal coloration of tungsten oxide, *Sol. Energy Mater. Sol. Cells* 90 (2006) 1945–1950.
- [24] H. Guo, N. Jiang, H. Wang, N. Lu, K. Shang, J. Li, Y. Wu, Degradation of antibiotic chloramphenicol in water by pulsed discharge plasma combined with TiO₂/WO₃ composites: mechanism and degradation pathway, *J. Hazard. Mater.* 371 (2019) 666–676.
- [25] F. Xu, K. Meng, B. Cheng, S. Wang, J. Xu, J. Yu, Unique S-scheme heterojunctions in self-assembled TiO₂/CsPbBr₃ hybrids for CO₂ photoreduction, *Nat. Commun.* 11 (2020) 1–9.
- [26] L. Hao, H. Huang, Y. Zhang, T. Ma, Oxygen vacant semiconductor photocatalysts, *Adv. Funct. Mater.* 31 (2021), 2100919.
- [27] J. Li, R. Lian, J. Wang, S. He, S.P. Jiang, Z. Rui, Oxygen vacancy defects modulated electrocatalytic activity of ironnickel layered double hydroxide on Ni foam as highly active electrodes for oxygen evolution reaction, *Electrochim. Acta* 331 (2020), 135395.
- [28] C. Guo, S. Yin, Q. Dong, T. Sato, The near infrared absorption properties of W₁₈O₄₉, *RSC Adv.* 2 (2012) 5041.
- [29] J.C. Hill, A.T. Landers, J.A. Switzer, An electrodeposited inhomogeneous metal-insulator-semiconductor junction for efficient photoelectrochemical water oxidation, *Nat. Mater.* 14 (2015) 1150–1155.
- [30] Y.F. Xu, X.D. Wang, J.F. Liao, B.X. Chen, H.Y. Chen, D.B. Kuang, Amorphous-TiO₂-encapsulated CsPbBr₃ nanocrystal composite photocatalyst with enhanced charge separation and CO₂ fixation, *Adv. Mater. Interfaces* 5 (2018), 1801015.
- [31] Y.-F. Xu, M.-Z. Yang, H.-Y. Chen, J.-F. Liao, X.-D. Wang, D.-B. Kuang, Enhanced solar-driven gaseous CO₂ conversion by CsPbBr₃ nanocrystal/Pd nanosheet schottky-junction photocatalyst, *ACS Appl. Energy Mater.* 1 (2018) 5083–5089.
- [32] Y. Jiang, J.-F. Liao, H.-Y. Chen, H.-H. Zhang, J.-Y. Li, X.-D. Wang, D.-B. Kuang, All-solid-state Z-scheme α -Fe₂O₃/Amine-RGO/CsPbBr₃ hybrids for visible-light-driven photocatalytic CO₂ reduction, *Chem* 6 (2020) 766–780.
- [33] X. Yang, S. Liu, J. Li, J. Chen, Z. Rui, Promotion effect of strong metal-support interaction to thermocatalytic, photocatalytic, and photothermocatalytic oxidation of toluene on Pt/SrTiO₃, *Chemosphere* 249 (2020), 126096.
- [34] J. Wang, S. Lin, N. Tian, T. Ma, Y. Zhang, H. Huang, Nanostructured metal sulfides: classification, modification strategy, and solar-driven CO₂ reduction application, *Adv. Funct. Mater.* 31 (2020), 2008008.
- [35] J. Kong, T. Yang, Z. Rui, H. Ji, Perovskite-based photocatalysts for organic contaminants removal: current status and future perspectives, *Catal. Today* 327 (2019) 47–63.
- [36] J. Ran, M. Jaroniec, S.-Z. Qiao, Cocatalysts in semiconductor-based photocatalytic CO₂ reduction: achievements, challenges, and opportunities, *Adv. Mater.* 30 (2018), 1704649.
- [37] M. Humayun, C. Wang, W. Luo, Recent progress in the synthesis and applications of composite photocatalysts: a critical review, *Small Methods* (2021), 2101395.
- [38] M. Xu, A. Zada, R. Yan, H. Li, N. Sun, Y. Qu, Ti₂O₃/TiO₂ heterophase junctions with enhanced charge separation and spatially separated active sites for photocatalytic CO₂ reduction, *Phys. Chem. Chem. Phys.* 22 (2020) 4526–4532.
- [39] S. Ji, Y. Qu, T. Wang, Y. Chen, G. Wang, X. Li, J. Dong, Q. Chen, W. Zhang, Z. Zhang, S. Liang, R. Yu, Y. Wang, D. Wang, Y. Li, Rare-earth single erbium atoms for enhanced photocatalytic CO₂ reduction, *Angew. Chem. Int. Ed.* 59 (2020) 10651–10657.
- [40] F. Yu, C. Wang, Y. Li, H. Ma, R. Wang, Y. Liu, N. Suzuki, C. Terashima, B. Ohtani, T. Ochiai, A. Fujishima, X. Zhang, Enhanced solar photothermal catalysis over solution plasma activated TiO₂, *Adv. Sci.* 7 (2020), 2000204.